Fundamental Understanding of Hingeless Hub Proprotor Stability

Nathan O'Brien
Clark School Fellow

Xavier Delgado
Graduate Research Assistant

Akinola Akinwale
Graduate Research Assistant

Anubhav Datta
Alfred Gessow Professor

Alfred Gessow Rotorcraft Center
University of Maryland
College Park, MD, USA

ABSTRACT

A 4.75-ft diameter hingeless hub tiltrotor model was developed and tested for aeroelastic stability up to a high speed of 200 knots corresponding to 468 knots full-scale. The model had interchangeable hubs, blades, and pylon center of gravity, allowing data acquisition for various new parametric variations. This paper documents the model, data and the insights gained from the test. The key conclusion is that a hingeless hub, when equipped with swept-tip blades, may significantly increase the stability compared to the state-of-the-art gimballed hub with straight blades. The causes were dissected using an in-house rotor comprehensive analysis to be the interaction of rotor regressive lag with wing-pylon modes, and the hub pitch and roll moments. The regressive lag was more important at lower speeds whereas the hub moments were more important at higher speeds. The torsion data was generally hard to measure and also hard to predict. Overall, the new data set shed light on high-speed tiltrotor flight and provided an unique database for validation of advanced rotor comprehensive analysis.

INTRODUCTION

High speed remains an important thrust area of research in vertical lift. Modern tiltrotors can fly at high speeds of 280 knots (kt) but the envisioned target of 400 – 450 kt still remains elusive.

The current tiltrotor hub is carefully crafted to support both helicopter and airplane modes of flight. The flexibility of the rotors needed for helicopter mode aggravates instabilities in the airplane mode. The current hub—the gimballed hub—is ideal for low loads in helicopter mode, but requires a thick wing, nominally 23% thickness to chord, to remain flutter-free in airplane mode. The thick wing undercuts the promise of the tiltrotor, and limits its cruise speed relative to a propeller aircraft which can afford a much thinner wing, of nominally 14% thickness to chord. To achieve 450 kt cruise, innovations are needed in hubs, blades and wings. The hub is the subject of this paper.

Hingeless hubs provide perturbation hub moments that may be stabilizing. The limiting case is a locked gimbal which leads to propeller whirl flutter at speeds far greater than the tiltrotor. But approaching that limit might generate structural loads beyond what helicopter flight can endure. Thus, the goal of a hingeless hub is to achieve gimbal locked-like stability in airplane mode with gimbal-free like loads in helicopter mode. However, there is a dearth of test data on hingeless hubs.

The only test data publicly available on hingeless hub is from a Boeing 26-ft diameter Model 222 (M222) rotor tested at the Ames 40- by 80-ft tunnel on a semi-span wing in 1972 (Ref. 1). The test measured loads and aeroelastic stability up to 192 kts. The wing-pylon was the same structure that a Bell 25-ft diameter gimballed rotor Model 300 was tested two years earlier (Ref. 2). A few years later, the William F. Putnam Company, Princeton, NJ, under contract from the the Boeing Vertol Company, Philadelphia, PA, designed and fabricated Froude-scale unpowered models of these rotors as part of NASA Contract NAS 2-8235 (report in June 1975, not in public domain). The Froude-scaled models had a 2.8-ft diameter and shared the same wing. The models were sent to MIT for gust loads measurements in the Wright Brothers tunnel (Refs. 3, 4). These were the first hub-interchangeable tiltrotor models. These models have since been destroyed and lost to history. An objective of this research is to build a new hub-interchangeable tiltrotor model, with modern instrumentation, an electric drive, and high-bandwidth electric actuation.

The development of the Maryland Tiltrotor Rig (MTR) and test data from its gimballed hub has been described in several recent papers (Refs. 5–10). This paper is focused on the new hingeless hub. The development of the hingeless hub and initial test data were published in Ref. 11. This paper documents the final results and insights gained from test and analysis.

Presented at the 50th European Rotorcraft Forum, Marseille, France, 10–12 September, 2024.

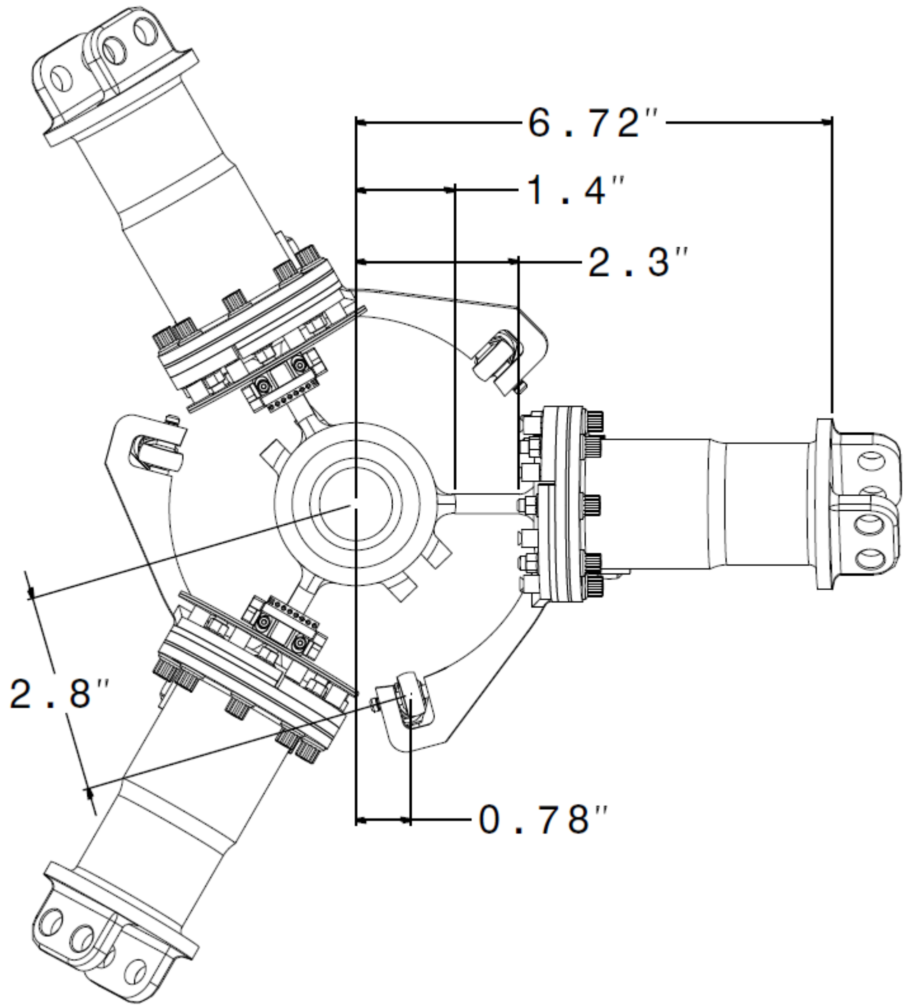

Figure 1: The hingeless hub top view showing the hub arm, pitch cases, and pitch horns; dimensions in inches

A 4.75-ft diameter hingeless rotor was tested for stability in airplane mode up to high speeds of 200 kt. Because it is loosely Froude-scaled to the Boeing 26-ft diameter rotor ($s = 1/5.33$), 200 kt corresponds to $200/\sqrt{s} = 468$ kt, albeit at low helical Mach numbers. The measurements were frequency and damping of wing beam, chord, and torsion motions. The results are compared with gimballed hub, gimbal-locked hub, swept-tip blades, and a new parameter—pylon center of gravity (C.G.). If the engine is fixed at the tip, and does not rotate with the pylon, this parameter can become important.

THE HINGELESS HUB

The general dimensions of the hingeless hub is shown in Fig. 1. The three-dimensional CAD drawing is shown in Fig. 2. The fabricated hardware is shown in Fig. 3.

The hub was designed to be softer in lag than the baseline gimballed hub; loosely resembling the Boeing M222 at Mach scale. It is also designed for the lag frequency to cut across 1/rev at a high rotor speed allowing both stiff- and a soft-inplane rotors to be studied. The present paper is limited to a Froude scale rotor speed of 1050 revolutions per minute (RPM). So the lag is stiff inplane. The values are given later.

The hub is designed to fit the same three-bladed pitch controls and swashplate geometry of the gimballed hub. It has the same 2° pre-cone. However, there is no kinematic pitch-flap coupling δ_3 as the effective flap hinge is outboard of the pitch bearing.

The main component of the hub is a central arm shown in Fig. 3a. It is made of AISI 4340 steel to provide adequate factor of safety at the target design frequencies. The frequencies are tailored by the rectangular flexbeam-like portion of the arms between the shaft collar end and the pitch case end. This portion is designed to make the rotor stiff in-plane at Froude scale and Mach-scale rotational speeds of 1050 and 2300 RPM respectively. The pitch bearings, cases and horns were made identical to the gimballed hub but duplicated for quick interchangeability. These components assembled onto the hub arm produced the interchangeable hub that could be re-connected to the same swashplate and drive system as shown in Fig 3b. More detailed description of the integration can be found in Ref. 11. Instrumentation was also duplicated, including a new

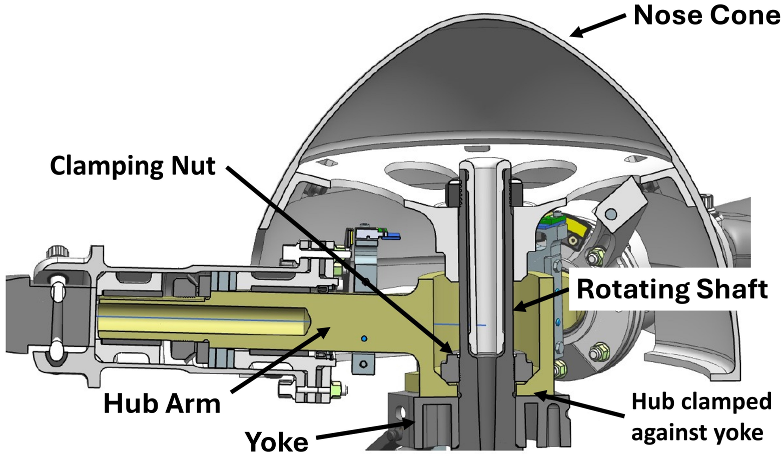

(a) Cross sectional view of the hub-shaft connection

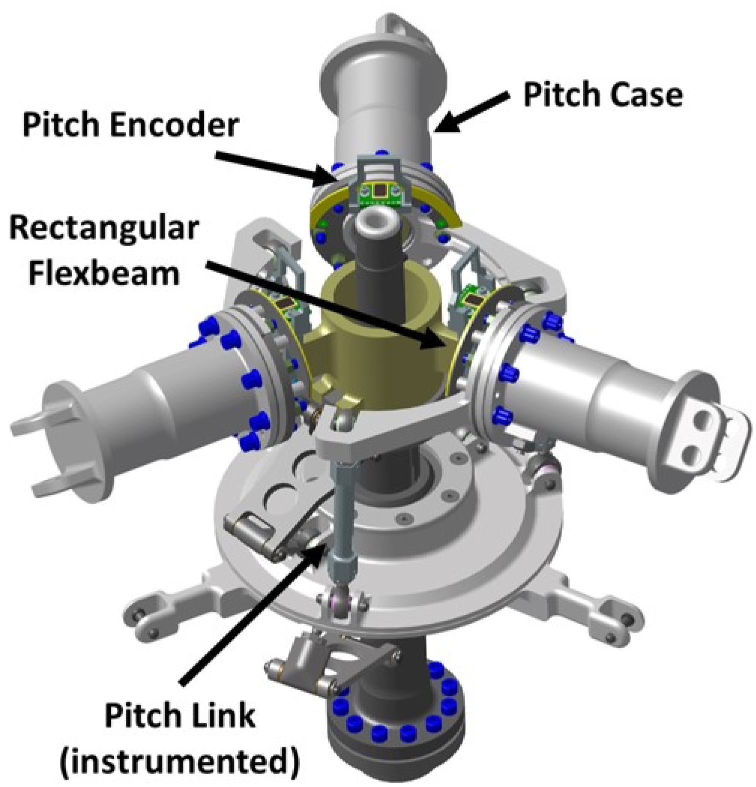

(b) Isometric View

Figure 2: The hingeless hub drawing.

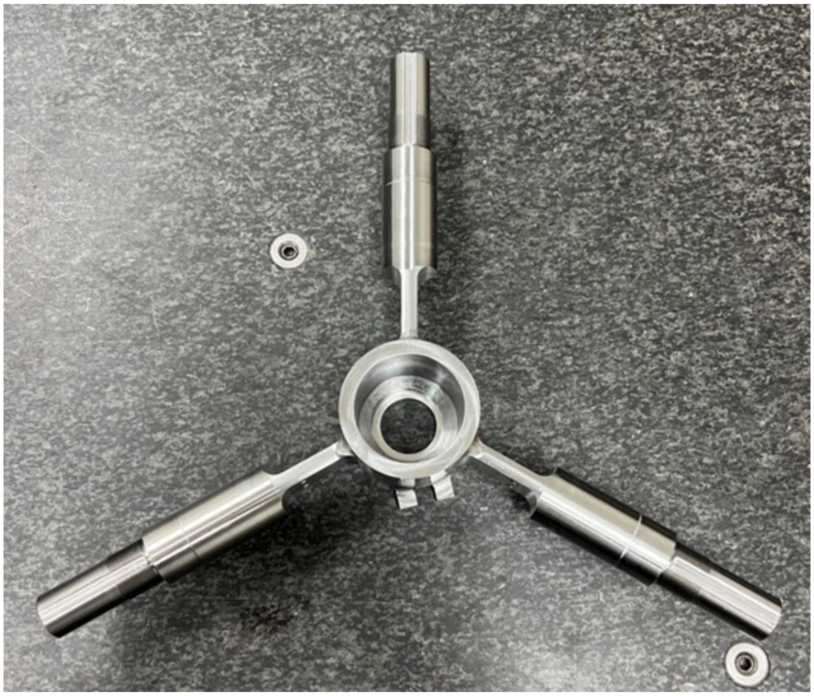

(a) The hub arms

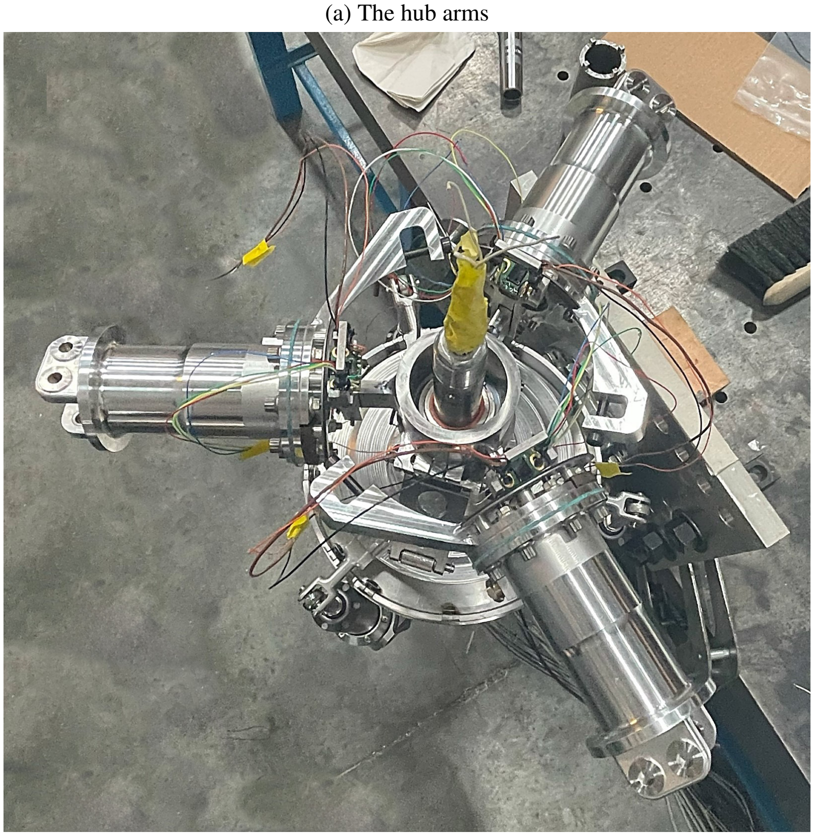

(b) Hub integrated on rig.

Figure 3: The Hingeless hub hardware.

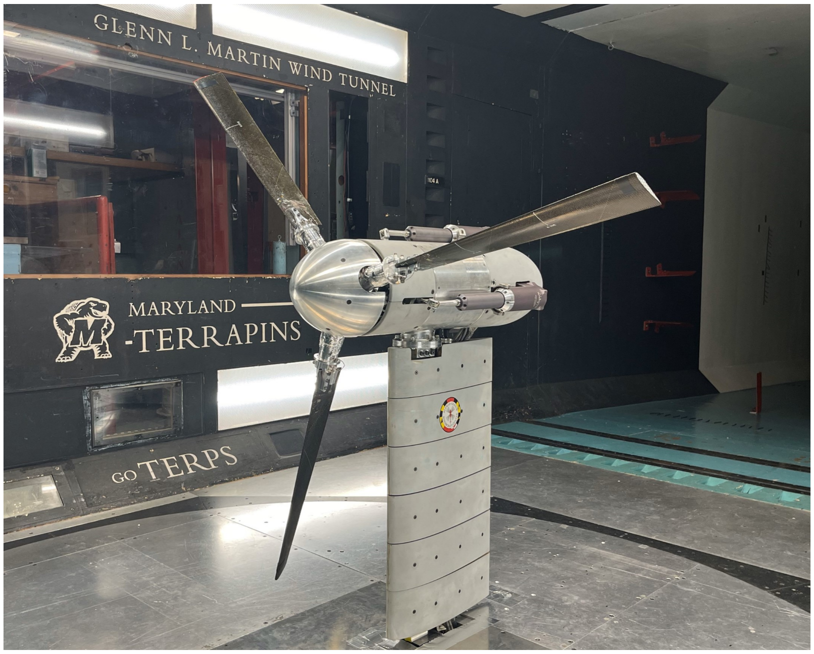

(a) Hingeless hub

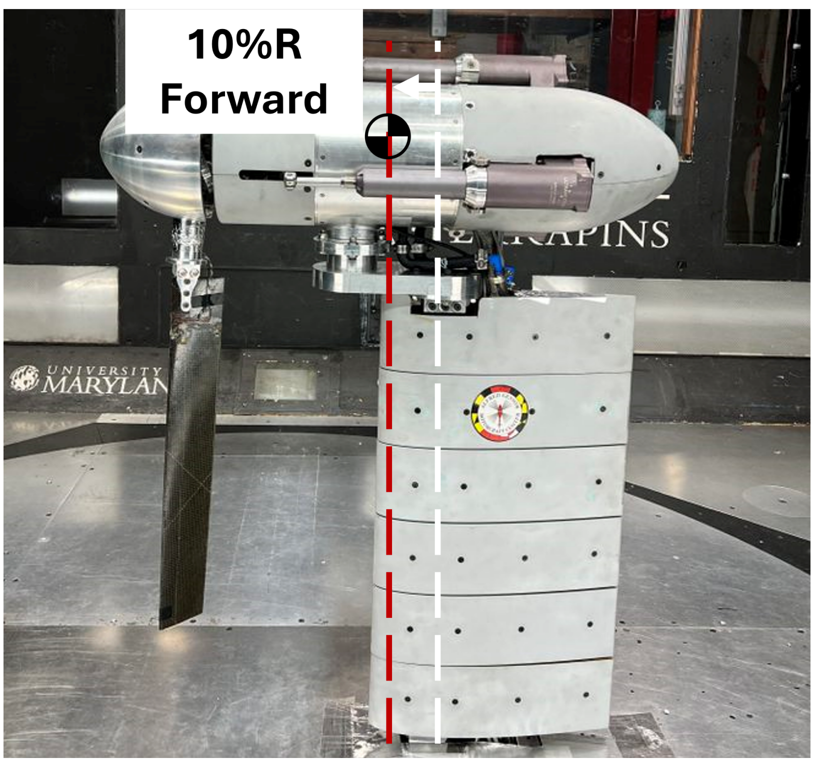

(b) Hingeless hub with forward pylon C.G.

Figure 4: Hingeless hub MTR installed in Glenn L Martin tunnel.

set of blade pitch sensors using RLC2IC magnetic encoders and RLS magnetic incremental rings, pitch link load strain gauges, a shaft torque gauge, and blade root strain gauges.

The slip ring, load cell and electric motor that are housed inside the pylon places it center of gravity (C.G.) 9.7 %R behind the wing spar (which is nominally the elastic axis). This is not typical of a tiltrotor aircraft where the C.G. is normally ahead of the elastic axis by $5-15$ %R. For example, the Bell 26-ft model had its C.G. ahead by 5 %R and the Boeing 25-ft model by 14.5 %R. In order to rectify this deviation a special adapter plate is built of Aluminum to bring the C.G. ahead of the wing spar by 10%R.

Table 1: MTR Rotor Properties

Number of blades	3
Radius, R	28.5 in
Blade chord	3.15 in
Twist	-37°
RPM (Froude)	1050
Rotor airfoil	VR-7
δ_3	0°
Blade sweep	0°, 20°
Sweep from	0.8 R
Floor clearance	0.195 R

WIND TUNNEL TESTING

The model with hingeless hub installed in the Glenn L. Martin Wind Tunnel is shown in Fig. 4a. The configuration with the C.G. adapter plate on is shown in Fig. 4b. The tunnel has a test section size of 7.75 by 11-ft and maximum speed of 200 kt.

Table 2: MTR Wing-Pylon Properties

Span	27.5 in
Chord	15.45 in
Airfoil	NACA 0018
Total Weight	66 lb
Natural Frequencies:	
Beam	5 Hz
Chord	9 Hz
Torsion	14.5 Hz
Structural Damping:	
Beam	0.24%
Chord	1.47%
Torsion	0.30%

The rotor properties are listed in Tab. 1. The rotor radius is 28.5 in. The distance from the hub to the tunnel floor is 34.05 in. So the rotor tip clearance from the floor is 5.55 in or 0.195 R which is about twice that of the V-22 clearance of 0.105 R. This is deliberate to allow shorter spars or longer blades in the future.

Table 3: Test Matrix

Test Number	Speed kt	Pitch θ_{75}, deg	RPM C.G.	Pylon
Straight:				
U10	30-200	11-57	1050	Standard
U11	30-200	11-58	1050	Forward
Swept-tip				
U12	30-200	11-57	1050	Standard
U13	30-200	11-58	1050	Forward

The wing properties are listed in Tab. 2. The wing airfoil begins about 5.5 in below the hub and spans 27.5 in ending about 1.0 in from the tunnel floor. The damping and frequencies of the installed system (non-rotating and wind-off) were measured by hammer tests. The hingeless hub weighs 7 lb compared to the gimballed hub which weighed 14.3 lb. The pylon and the blades remain the same, weighing 57 and 2 lb respectively. The pylon adapter weighed 6 lb. When used, the change in frequencies or damping were not that significant.

The test matrix is given in Tab. 3. Four speed sweeps were carried out designated $10-13$. The naming convention follows Ref. 6 with the location, sweep number, and tunnel speed to describe a sweep. For example, N1.78 referred to the test points collected at the Navy tunnel (hence N), in the first speed sweep (hence 1) and at 78 kt. Here U11.180 would mean test points collected at the University of Maryland (hence U), in the 11-th speed sweep at at 180 kt.

The tests were conducted in the freewheeling mode. At each speed, the collective pitch was trimmed to achieve the target RPM. The Froude-scale RPM corresponding to the M222 is 903. But there was torsion resonance at this RPM (torsion frequency 14.5 Hz = 870 RPM). To avoid this, the Froude-scale RPM corresponding to the gimballed hub was retained. So the target RPM was 1050. This allowed consistent comparison of the gimballed and hingeless rotors later. The cyclic pitch was trimmed to minimize hub moments. Ideally, moments should be zero in axial flow, but blade dissimilarities produced a small moment. The blade tracking was checked with strobe light reflecting off colored tapes glued at the blade tips. If the blades were out of track (by more than 1/2-thickness) the test was stopped and pitch links adjusted.

Once trim solution was attained, the model was perturbed with high bandwidth swashplate actuators. Because the actuators are in the fixed frame, they were actuated near the model natural frequencies. The actual flutter frequencies would be close to these natural frequencies. The wing beam and torsion modes were both perturbed using a longitudinal cyclic θ_{1s} at the wing-pylon natural frequencies. The chord mode was perturbed using the collective θ_{75}. Five cycles of actuation were introduced with nominal values of 5.4° for beam, 2° for chord, and 0.1° for torsion. At least three (and up to five) trials were taken for each condition.

The blades were fabricated in-house following the procedure laid out in Ref. 7. The layup is ±45° so there is no material coupling. The swept-tip blades were identical to the straight blades except for a 20° sweep at the outer 20% R.

The swept-tip portion did not have an internal spar. The airfoils are placed along the swept quarter-chord. The goal of the swept-tip blades was to impact dynamics through aerodynamic pitch flap coupling. The blades were first tested on the gimballed hub and reported in Refs. 9 and 10. They were refurbished for the new hingeless tests.

DAMPING CALCULATION

Wing mounted strain gauges recorded strains versus time over a period of 10 seconds at a sample rate of 10 kHz. The record included a portion of the initial steady-state, followed by the actuation stage, and then the decay stage. This record was down sampled to 1 kHz for ease of storage. Damping was calculated from this signal.

Damping was calculated from the decay stage using Moving block and Prony methods. The theory of Moving block method assumes the damped frequency to be equal to the natural frequency, i.e., $\omega = \omega_n\sqrt{1-\zeta^2} \approx \omega_n$, so it is typically applicable for damping less than 5%, i.e., $\zeta \leq 0.05$. But the method is robust to noise. The alternative at higher damping is to use Prony but it can be quite sensitive to noise. It was important to filter out the /rev frequencies from blade dissimilarities, even when small, and the noise, as much as possible, before extraction of damping. The overall scheme illustrated below.

Consider a typical set of wing strain signals from beam, chord and torsion mode excitation as shown in Figs. 5, 6, 7. These are taken from U11.100. The data was first cleaned using an infinite-impulse response (IIR) notch filter to remove all /rev frequencies. Filtering is especially vital for torsion data as the wing torsion frequency of 14.5 Hz equals 0.83/rev hence near 1/rev. Blade dissimilarities produce some 1/rev and the torsion signal, already the weakest of all signals due to reduced actuation authority, lies hidden. Low-pass and high-pass filters were used next to remove certain undesired frequencies as well. The data after filtering are shown in Figs. 8, 9, 10. The steady-state, perturbation, and decay are now clearly visible.

The torsion signal from Fig. 10 is re-plotted in Fig. 11 with the steady-state, actuation, and decay marked. A 1024 sized sample window of 1.024 seconds ($\Delta t = 0.001$ s) of the decay stage is selected as shown in Fig. 12. A 512 sized block is selected and shifted, or moved, along the decay window from the first to the last possible block. Figure 13 highlights the first, the 256-th, and the last block that fit within the 1024 sized decay window. A Fast Fourier Transform (FFT) is performed within each block to find the largest amplitude and corresponding frequency. This frequency is the damped frequency $\omega \approx \omega_n$. The natural log of the amplitude when plotted versus the starting time of each block appears as Fig. 15. The slope of the linear fit slope is $\zeta\omega_n$ where ζ is the damping ratio and ω_n is the natural frequency. Thus ζ is calculated.

The Prony method uses a series of sinusoids to reconstruct the signal. The order of the sinusoidal functions is denoted as M. In this case $M = 300$ gave the best regression fit (minimum root mean square error). The result is shown in Fig. 16.

COMPREHENSIVE ANALYSIS

The new University of Maryland Advanced Comprehensive Code—version 2 (UMARC-II) was used as the baseline analysis platform (Refs. 8, 12).

Properties: The blade mass and stiffness properties were measured. The root-end properties were calculated using commercial FEA. The pylon moments of inertia were not measured with the new hub, so the gimballed values given in Ref. 6 were retained. Only the mass was updated to reflect the lighter hingeless hub. The wing structural properties were based on the measured frequencies and damping in Tab. 2. The airfoil properties of the blade and wing were obtained from in-house CFD as a C-81 deck. The wing is segmented, which is typical of any flutter model, but considered continuous in the analysis. The segmented wing allows friction to kick in should sudden instabilities appear but the gaps are small enough to prevent three-dimensional flows.

Model: Because the lay-up is symmetric, isotropic Euler-Bernoulli beam finite elements could be used to model the rotor. Each blade was modeled with 18 elements. Figure 17 gives these properties. The rotor fan plot is shown in Fig. 18. The hingeless frequencies are the solid lines. There is no test data for validation. However, there is test data for the gimbal locked condition (Ref. 13). These are the dashed lines. The hingeless hub is hard to reproduce in the vacuum chamber rotor rig, but because the blades are identical the model is considered validated as far as possible. At 1050 RPM, the lag frequency for the hingeless hub is around 1.6/rev, and the flap frequency 3.5/rev. At 2400 RPM, the lag mode would cross over from stiff- to soft-inplane, and the flap frequency would be around 1.8/rev.

The wing is already isotropic. The wing itself is modeled with 10 elements. The adapter plate was simply a C.G. shift. The stiffness and inertia of the adapter plate are important, but left out of this preliminary model. The pylon and hub connection is modeled with 2 structural elements.

A lifting-line aerodynamic model is used, with uniform inflow for the wake. The inflow ≈ 0 in airplane mode so a refined wake model is usually not needed. Analysis with free wake confirmed no effect of the wake (Refs. 8, 12). Linear unsteady aerodynamics is used. It is not needed on the wing (as the reduced frequency is quite low) but retained nevertheless for consistency with the rotor.

Solution procedure: First, the rotor is trimmed in freewheeling — collective found for zero torque at the tunnel speed. The predicted and measured collectives are compared in Fig. 19. The measurements are similar for all blades. Predictions are satisfactory.

Once trimmed, eigenanalysis is used to find the stability roots. The rotor equations are converted to multiblade coordinates to allow eigenanalysis. The solution was verified with a transient analysis with the rotor equations in the rotating frame. The transient option is easier for the gimballed hub but would not produce a solution if the model were to be unstable.

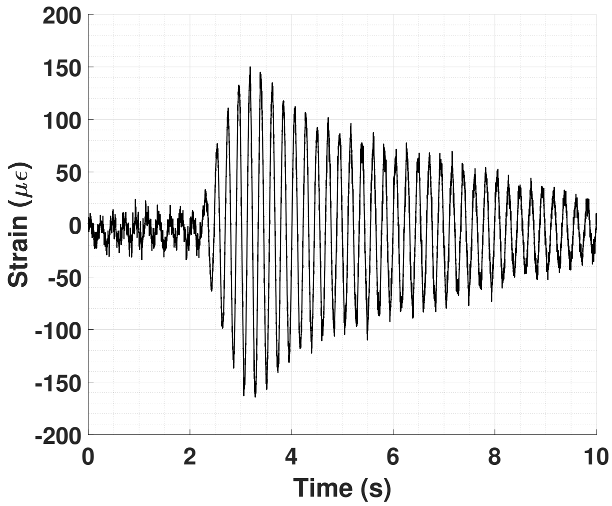

Figure 5: Beam strain signal.

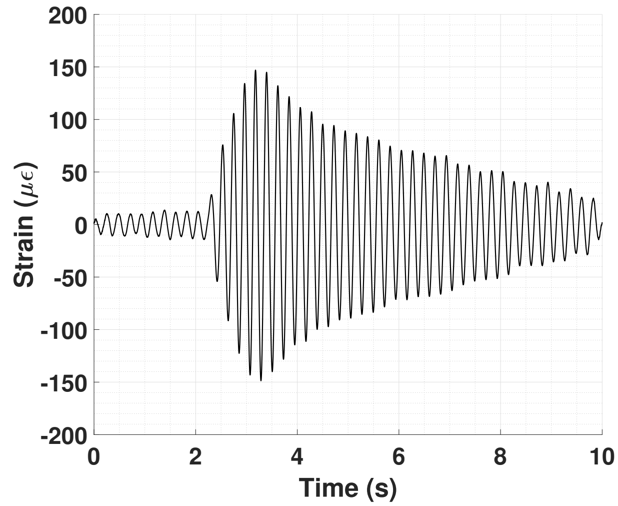

Figure 8: Filtered beam strain signal.

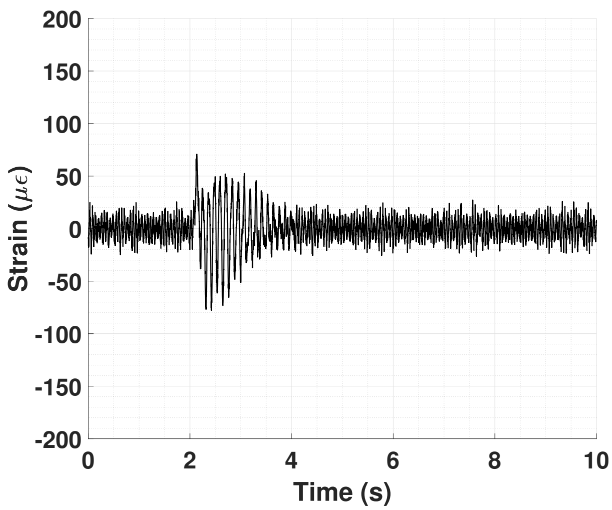

Figure 6: Chord strain signal.

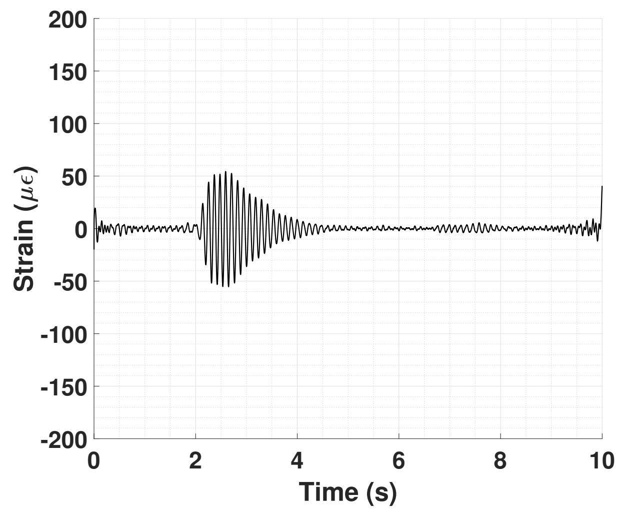

Figure 9: Filtered chord strain signal.

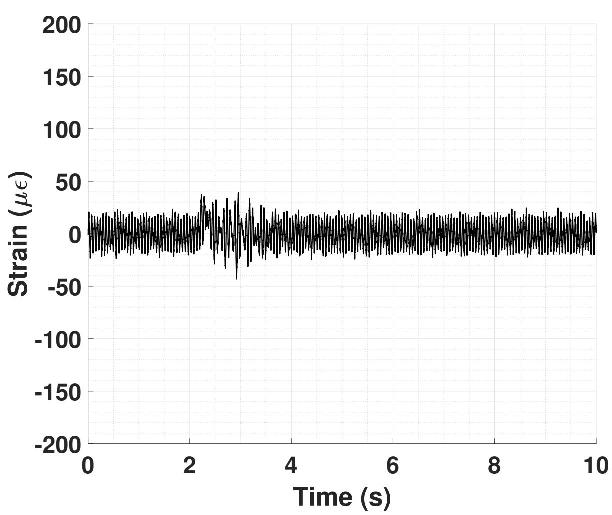

Figure 7: Torsion strain signal.

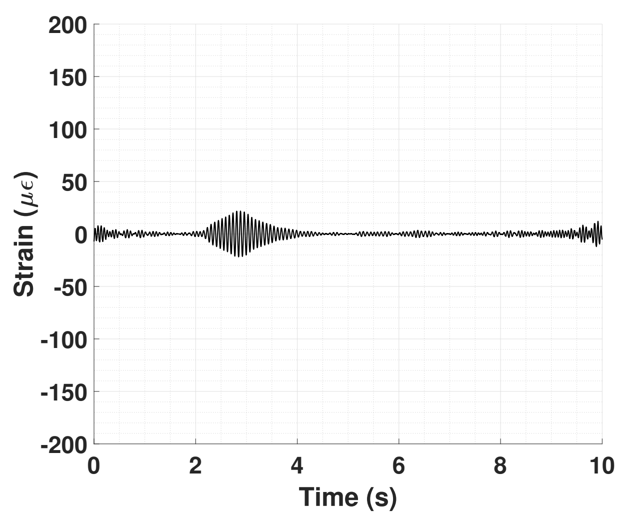

Figure 10: Filtered torsion strain signal.

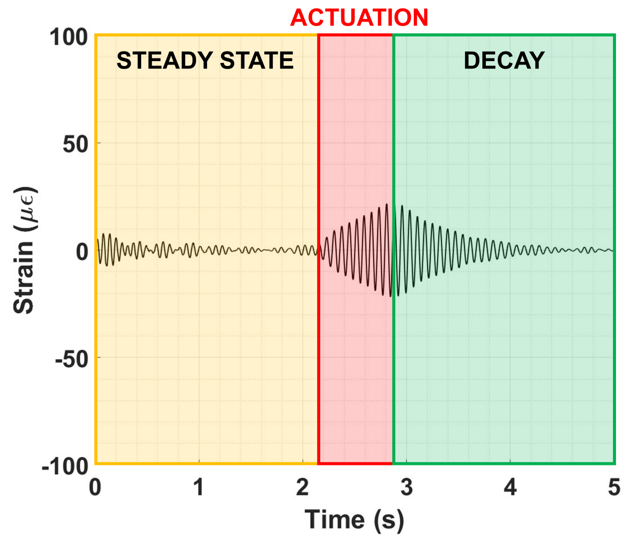

Figure 11: Torsion strain showing steady-state, actuation, and decay.

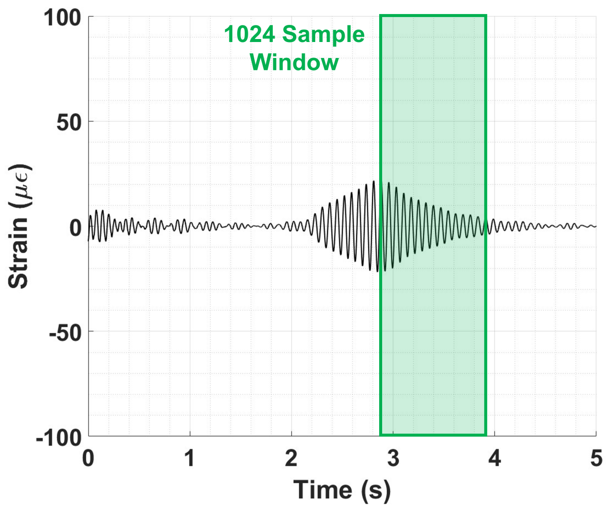

Figure 12: Decay window.

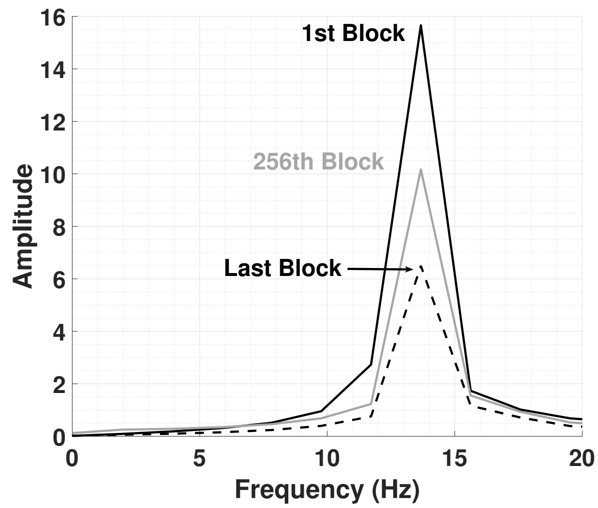

Figure 14: Amplitude of moving blocks.

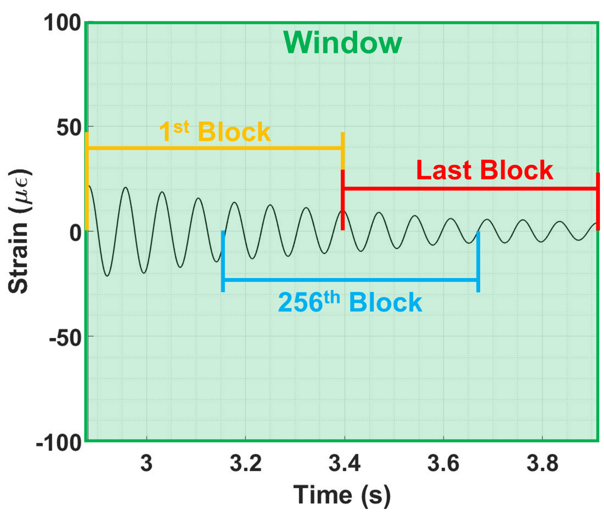

Figure 13: Moving blocks within decay window.

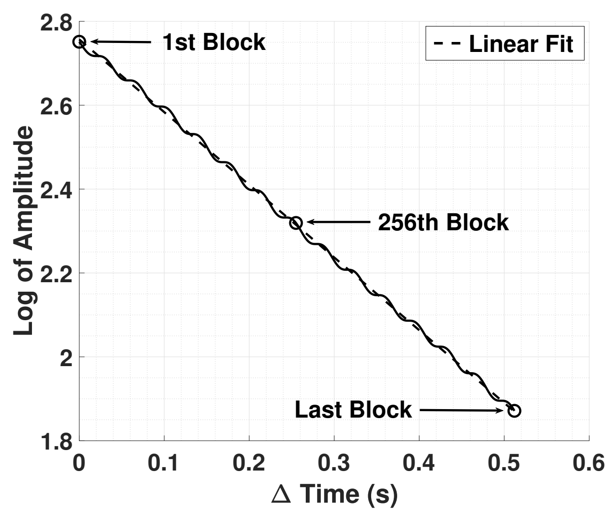

Figure 15: Natural log of amplitude versus block time.

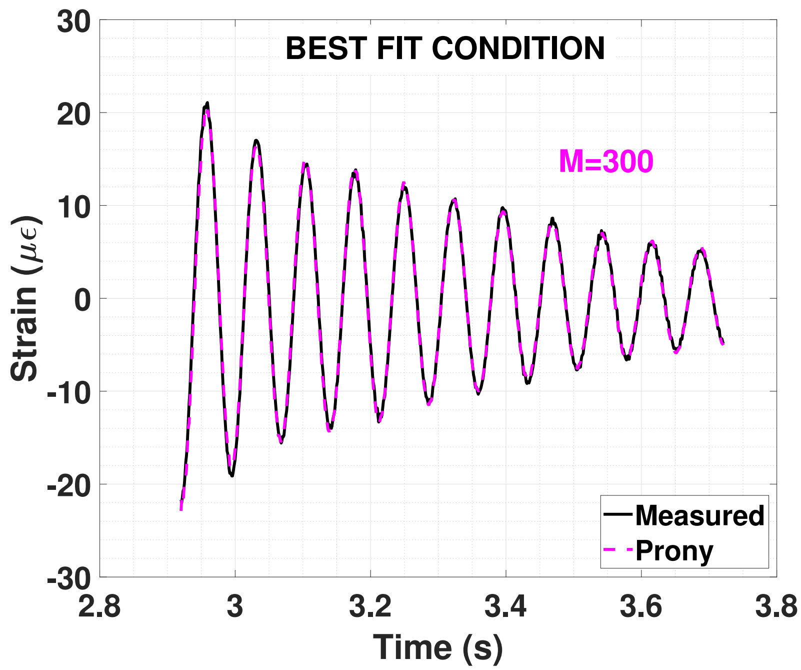

Figure 16: Prony approximation to torsion signal; $M = 300$.

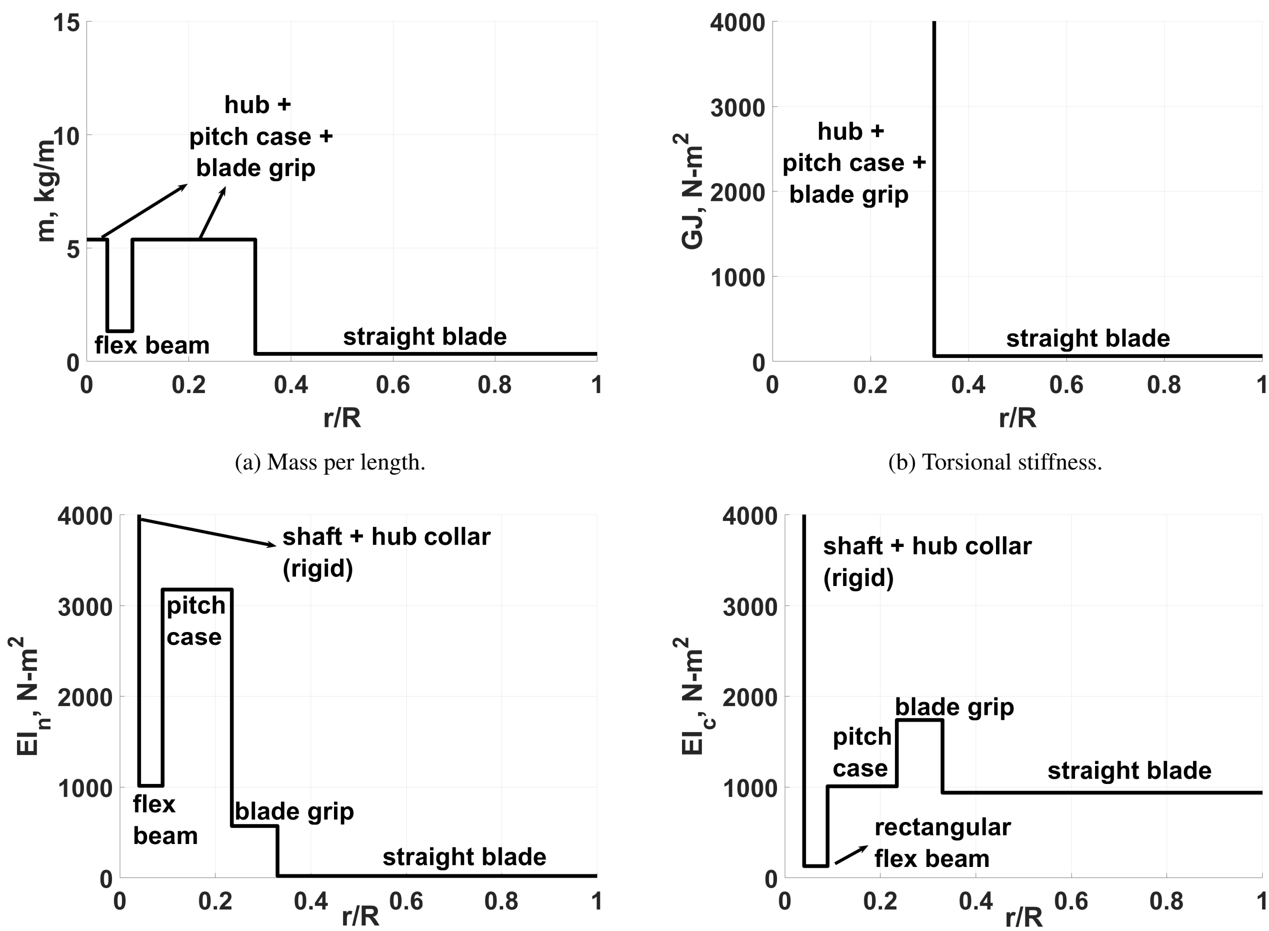

(a) Mass per length.

(b) Torsional stiffness.

(c) Normal bending stiffness.

(d) Chordwise bending stiffness.

Figure 17: Structural properties of the hingeless rotor.

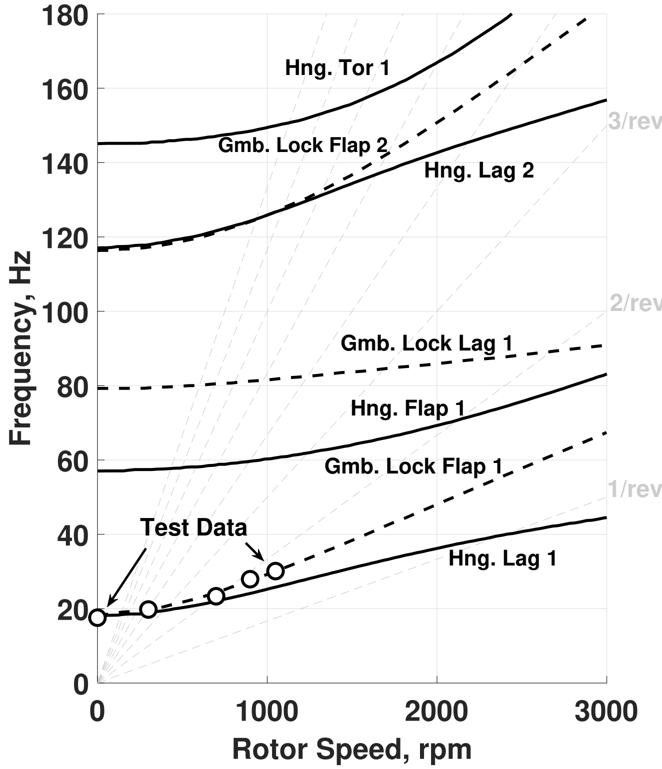

Figure 18: Hingeless hub at 40° collective.

MEASURED DAMPING

The damping from the baseline model is shown in Fig. 20. The baseline model is with straight blades and without the pylon C.G. adapter. The beam damping is the lowest, with an increasing trend with speed, and a drop off as it approaches 200 kt. The next higher mode is torsion, with a relatively flat trend. Finally there is chord damping, which is the highest, with a rapidly decreasing trend between $30-100$ kt, and relatively flat thereafter.

A curious change in behavior is noticed when the straight blades are replaced with swept-tip blades. The damping is shown in Fig. 21. The chord and the torsion now appear flipped. The chord is now the next higher mode from beam, with a relatively flat trend, whereas torsion has the highest damping, with a rapidly decreasing trend between $30-100$ kt. Note that all other parts of the model has remained the same, only the blades were replaced. The blades were identical as well, except only the swept-tip.

The C.G. shifted configurations do not change this general behavior. The straight blades still show chord with the highest damping (Fig. 22) and the swept-tip flips this behavior with torsion with the highest damping (Fig. 23). The main change appears to be a large amount of scatter in torsion data, for reasons that are not clear. There also seems to be a sharp rise in torsion damping at high speed but conclusions are premature with this level of scatter.

The curious behavior of chord and torsion flipping trends can be explained by comparing measured data with predictions in

!

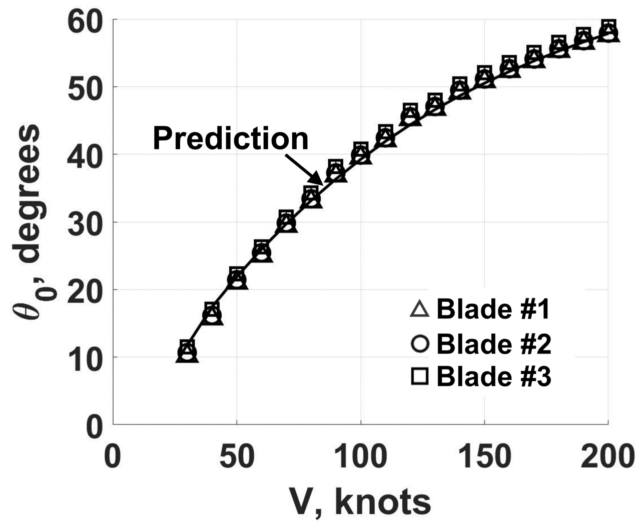

Figure 19: Measured and predicted collective pitch.

the following section.

DATA VERSUS PREDICTIONS

Comparing data with predictions from comprehensive analysis provides a check for that data and validation for the analysis.

Consider the baseline configuration first. The baseline configuration has straight blades. The predicted frequencies are shown in Fig. 24. The wing-pylon beam mode is denoted as q_1, chord as q_2, and torsion as p. The test data are shown as symbols and predictions as lines. The frequencies remain well separated throughout. The rotor flap (first mode) and lag (first mode) frequencies are that of corresponding multiblade coordinates. The standard notations of β and ζ denote the collective flap and lag respectively. So $\beta+1$ and $\zeta+1$ are the high frequency flap and lag modes respectively and $\beta-1$ and $\zeta-1$ are the low frequency flap and lag modes respectively. These frequencies are hard to measure, hence predicted values play a key role in fundamental understanding. It is clear that the low frequency lag mode (in this case regressive) is very close to the chord mode. The lag mode is very well damped in airplane mode due to high inflow, and this damping is transferred to the chord mode.

Now consider the swept-tip blades. The predicted frequencies are shown in Fig. 25. The sweep at the tip provides a greater stiffness in lag motion from a larger restoring moment. This increases the lag frequency so that the regressive lag is now very close to the torsion mode. Therefore the damping is now transferred to the torsion mode. This explains the curious behavior of chord and torsion modes flipping. This also shows that a swept-tip can have other effects beyond pitch flap coupling alone.

Attention is focused next on damping.

Consider first the baseline configuration again. Figure 26 shows the beam damping. Predictions are satisfactory up to

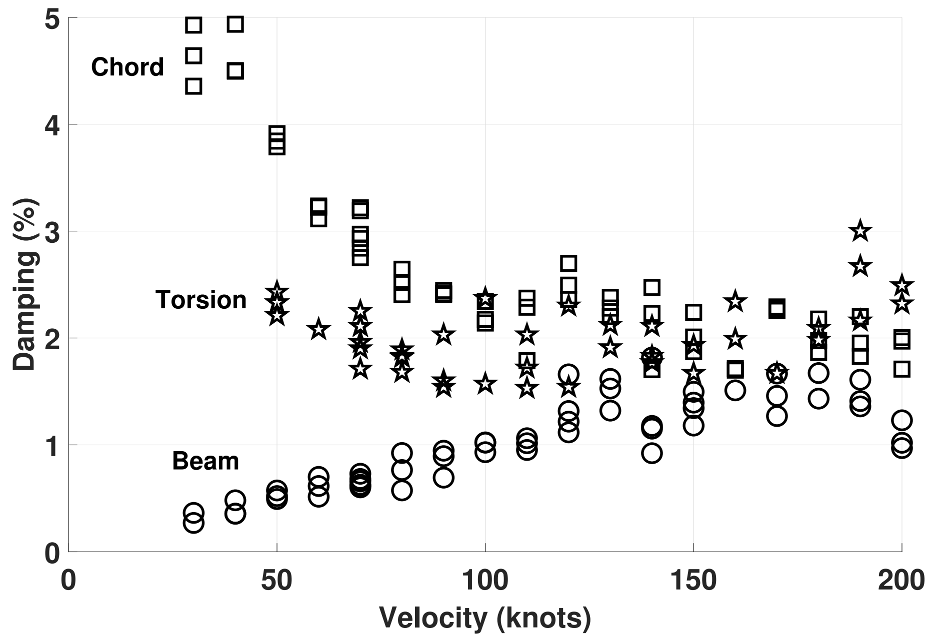

Figure 20: Damping; straight blade.

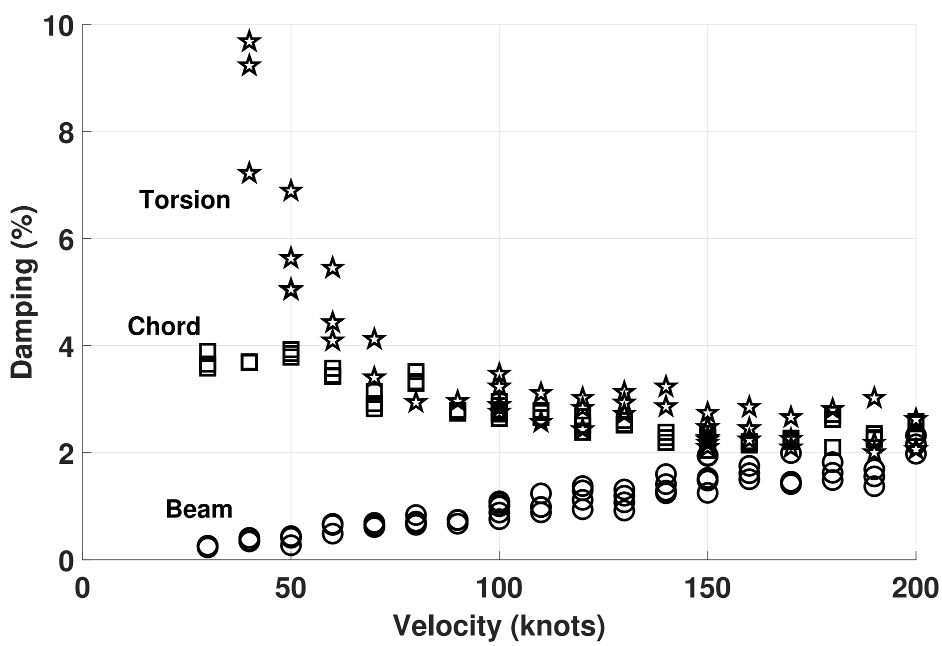

Figure 21: Damping; swept-tip blade.

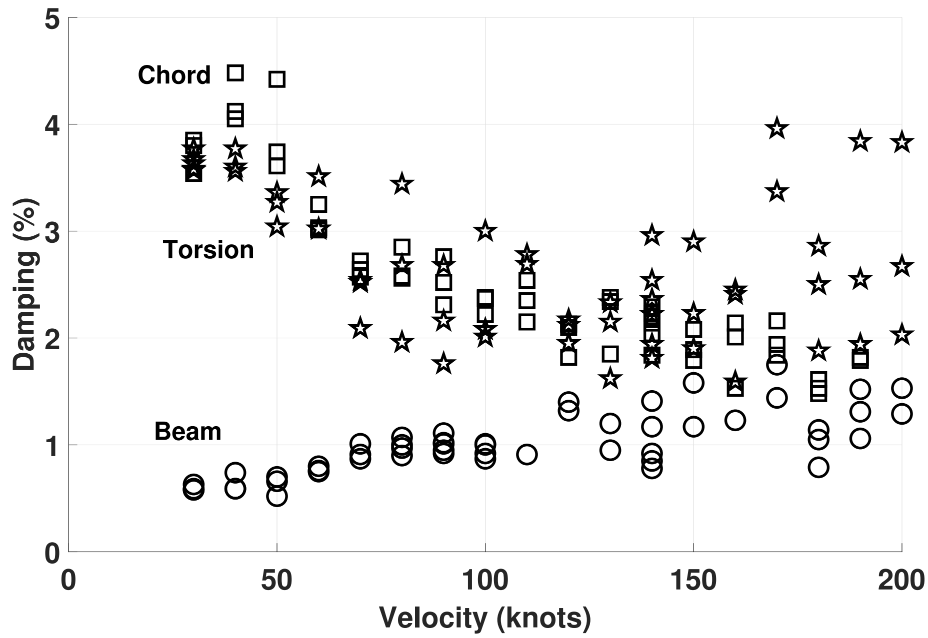

Figure 22: Damping; straight Blade, pylon C.G. 10 % R forward of wing spar.

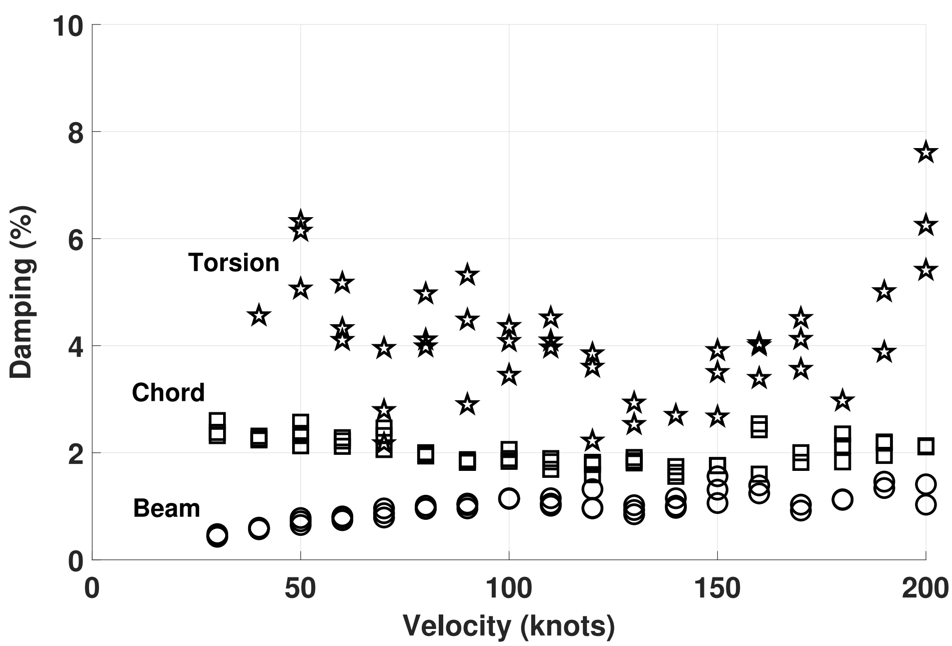

Figure 23: Damping; swept-tip blade, pylon C.G. 10 %R forward of wing spar.

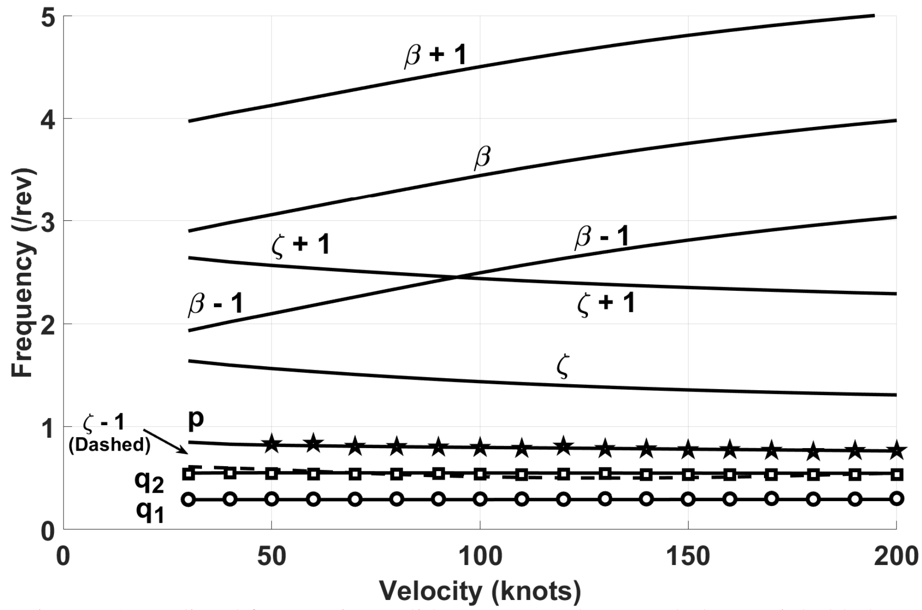

Figure 24: Predicted frequencies (solid) versus test data (symbols); straight blades.

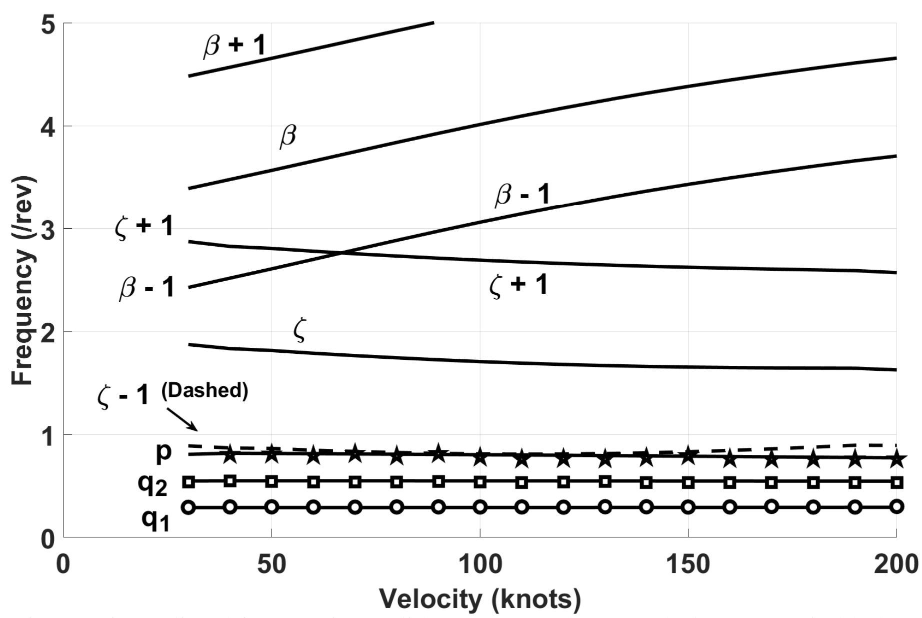

Figure 25: Predicted frequencies (solid) versus test data (symbols); swept-tip blades.

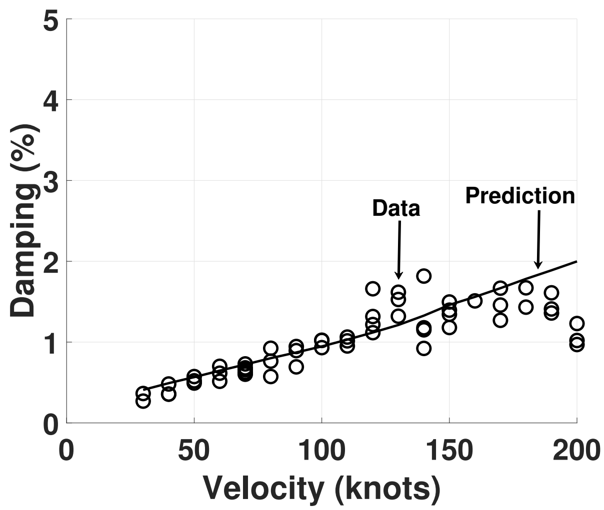

Figure 26: Beam damping; straight blade.

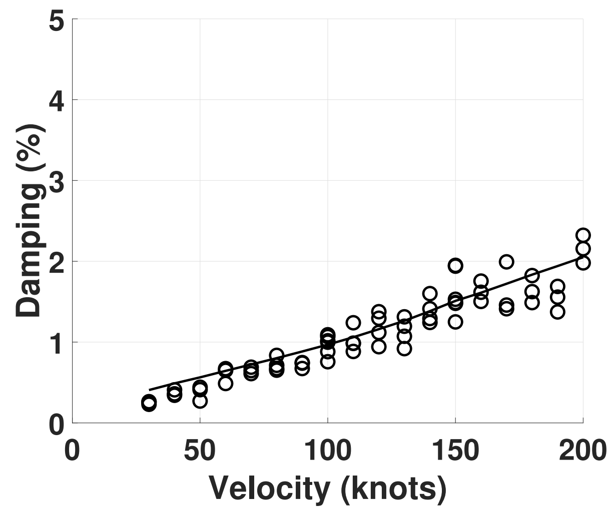

Figure 29: Beam damping; swept-tip blade.

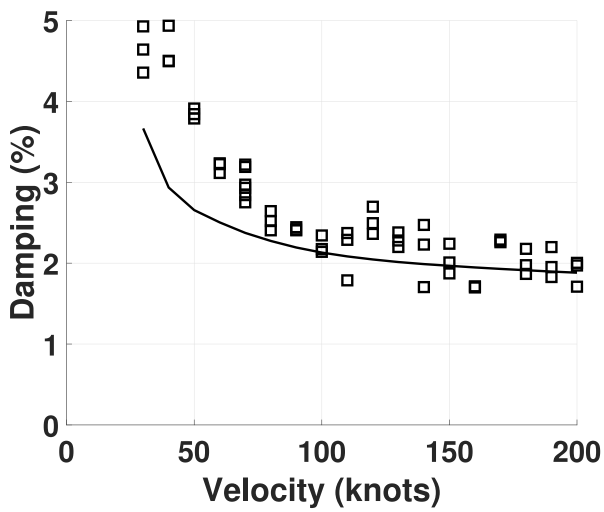

Figure 27: Chord damping; straight blade.

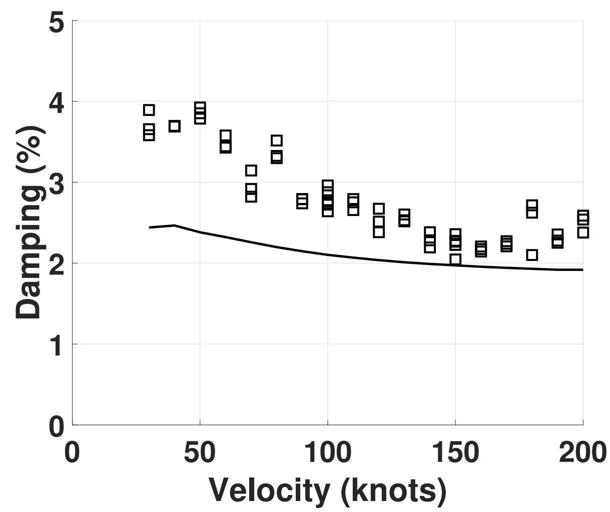

Figure 30: Chord damping; swept-tip blade.

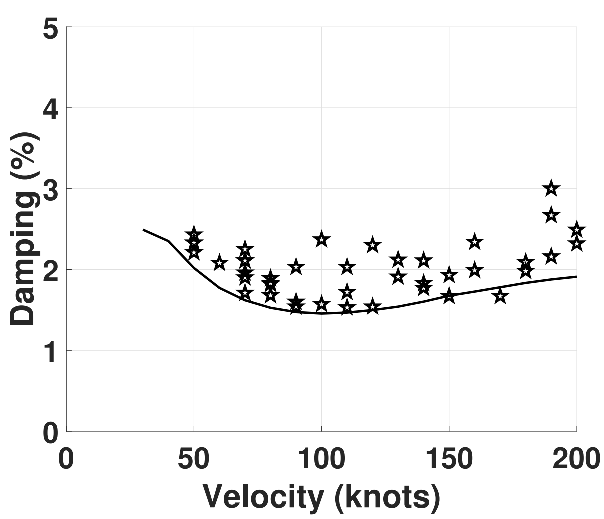

Figure 28: Torsion damping; straight blade.

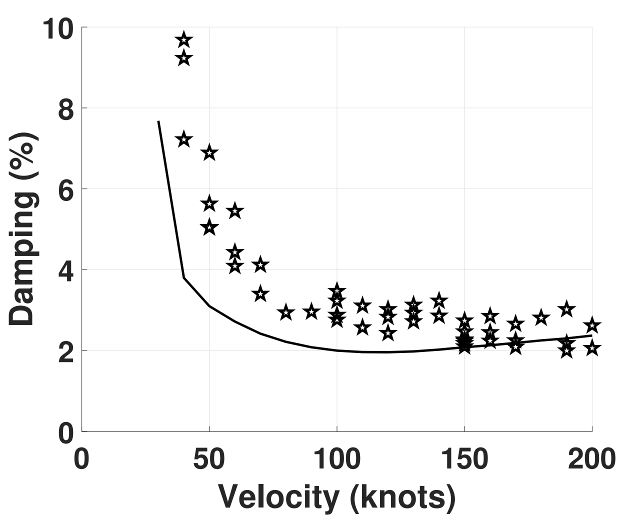

Figure 31: Torsion damping; swept-tip blade.

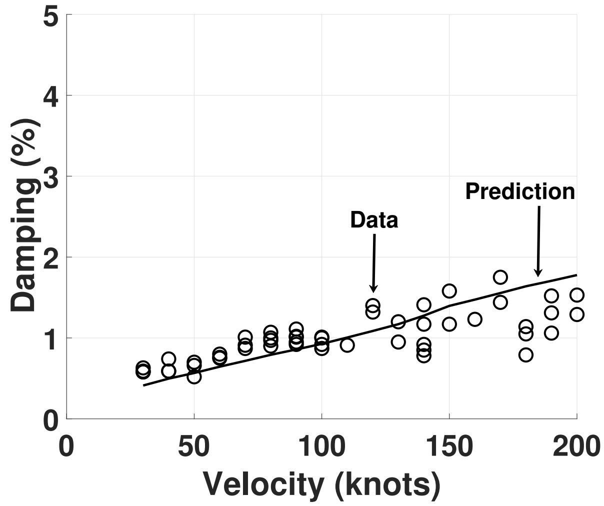

Figure 32: Beam damping; straight blades; C.G. shifted.

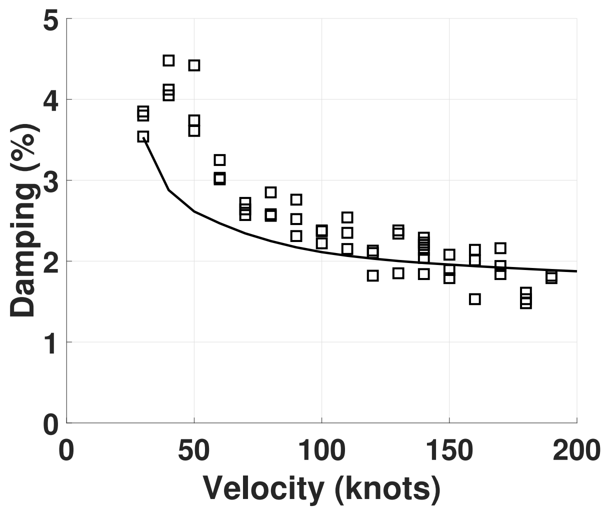

Figure 33: Chord damping; straight blades; C.G. shifted.

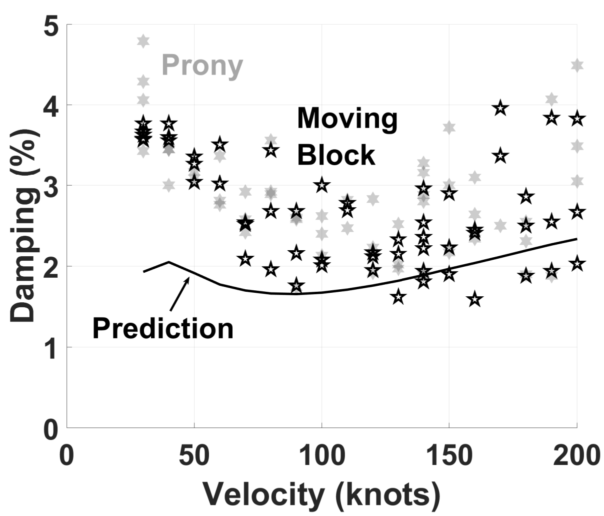

Figure 34: Torsion damping; straight blades; C.G. shifted.

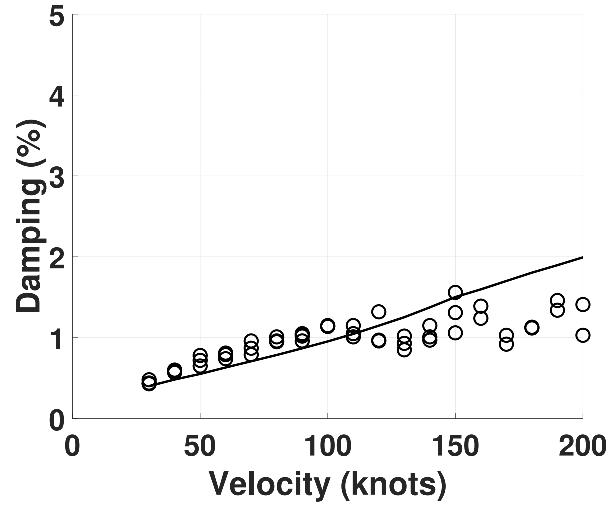

Figure 35: Beam damping; swept-tip blades; C.G. shifted.

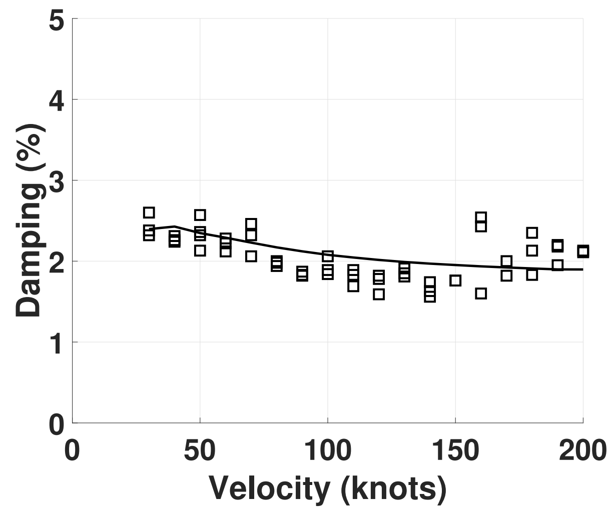

Figure 36: Chord damping; swept-tip blades; C.G. shifted.

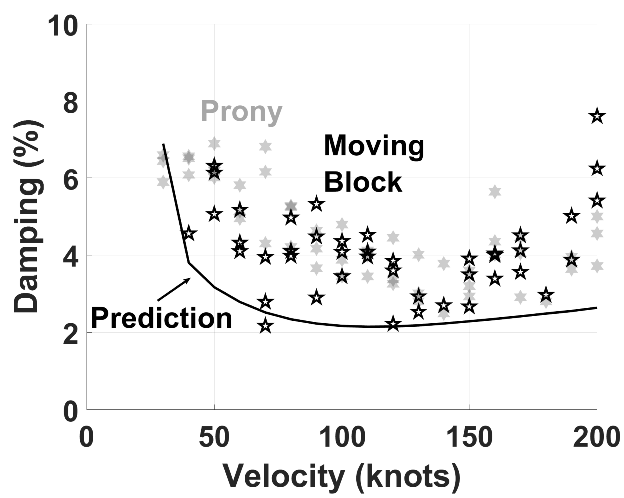

Figure 37: Torsion damping; swept-tip blades; C.G. shifted.

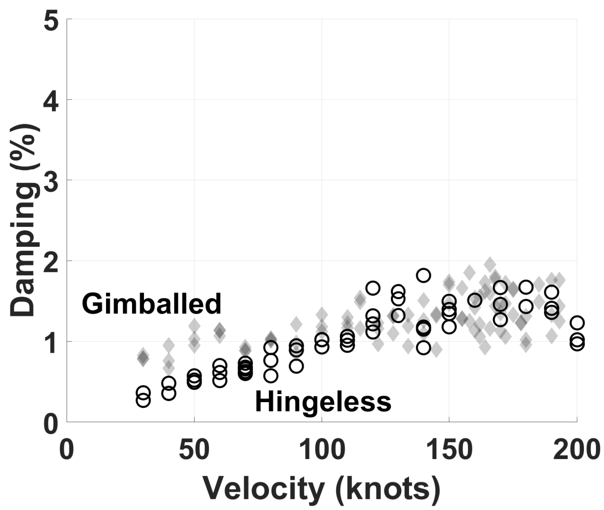

Figure 38: Beam damping; hingeless versus gimballed.

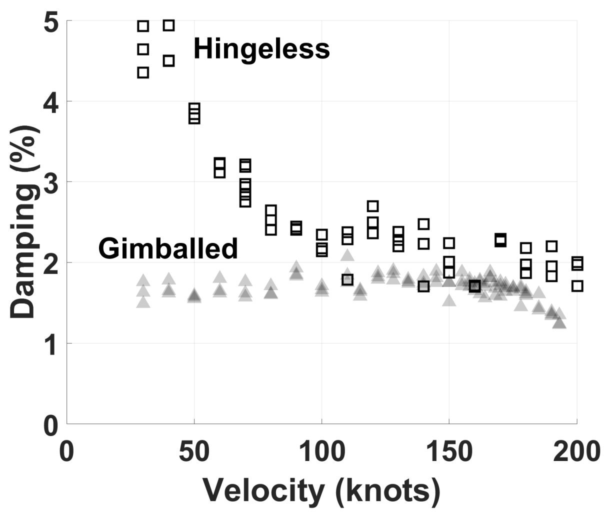

Figure 39: Chord damping; hingeless versus gimballed.

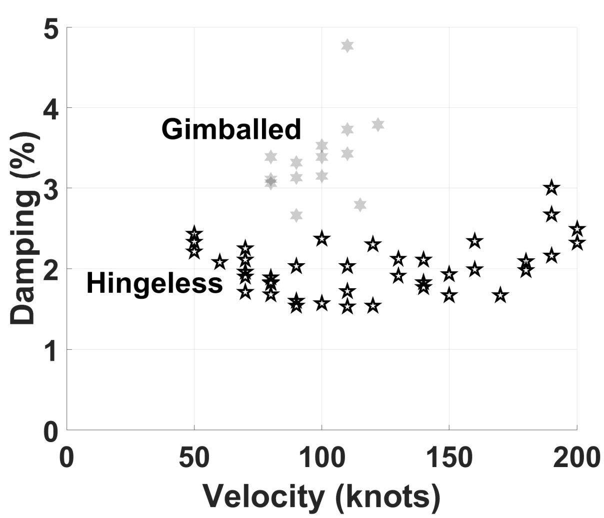

Figure 40: Torsion damping; hingeless versus gimballed.

180 kts, but the drop that appears to occur at 190 kt and continues to 200 kt is not predicted. Figure 27 shows the chord damping. The rise in damping due to the regressive lag is predicted by the analysis although the magnitude of prediction is not very satisfactory. Figure 28 shows the torsion damping. Predictions are reasonable, with the capture of the downward trend up to 120 kt followed by a gradual increase. There is a slight under prediction across all speeds.

Now consider the swept tip. Figure 29 shows the beam damping. It is similar to the baseline. Figure 30 shows the chord damping. The proximity to regressive lag is gone and so neither the data nor the predictions show the peak at low speed. The magnitude error remains so the predictions are not very satisfactory. Figure 31 shows the torsion damping. Recall, the regressive lag is now close to the torsion mode. The rise in damping due to this proximity is predicted by the analysis.

Next consider the C.G. shifted configuration.

Consider the same sequence, first the straight blades, then the swept-tip.

The beam, chord, and torsion damping for the straight blades are shown in Figs. 32, 33, and 34 respectively. There is no change in beam and chord results; the problem is with torsion. The torsion data is shown extracted with two different methods both of which show a high scatter. Nevertheless it is clear that the damping is higher at low speeds than before. But the analysis does not pick up this trends; the predicted damping does not change significantly from before (Fig. 28). Perhaps this suggests the adapter piece must be modeled properly, with inertia and stiffness, and not just considered a C.G. offset.

The beam, chord, and torsion damping for the swept-tip blades are shown in Figs. 35, 36, and 37 respectively. Recall, the principal change in physics is the shift of the regressive lag toward torsion. Because it is well predicted, there appears to be less problem with torsion. The data in torsion still show a high scatter, although the Prony analysis appears to show a little less scatter. Even though the trend is captured, the magnitudes are under predicts throughout the speed range.

FUNDAMENTAL UNDERSTANDING

To gain a clearer understanding of the stability of a hingeless hub and swept-tip blades compared to the more traditional gimballed hub and straight blades, three parametric variations are studied: 1) hingeless versus gimballed hub, 2) hingeless versus gimbal-locked hub, and 3) straight versus swept-tip blades. The baseline pylon C.G. location is considered for all. The hingeless hub results are new here. The gimballed and gimbal-locked results are re-produced from Refs. 9, 10.

Hingeless versus gimballed hub: Consider straight blades. Figures 38, 39, and 40 compare damping in beam, chord, and torsion modes respectively. In the beam mode there is no significant change. In the chord and torsion modes the changes are significant. This is generally expected as the hub moments would affect these modes—hub roll (or airplane yaw)

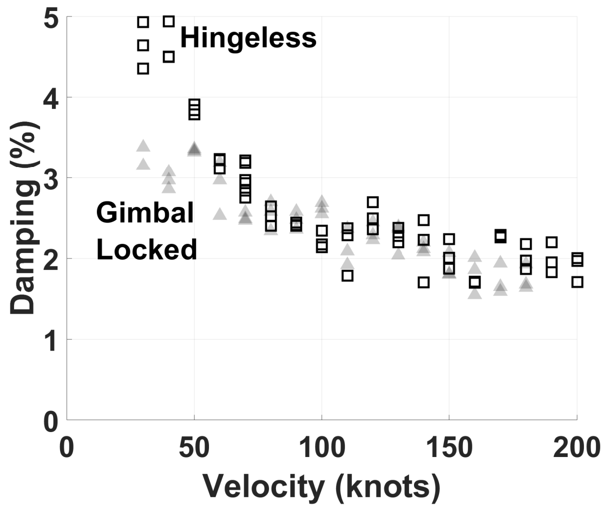

Figure 41: Chord damping; hingeless versus gimbal-locked.

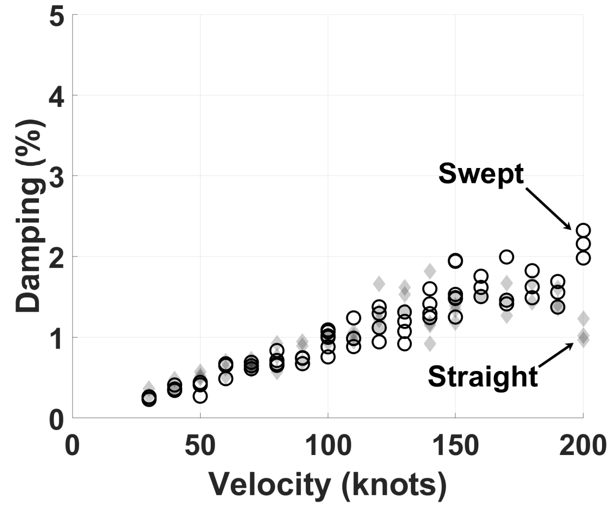

Figure 42: Beam Damping; swept versus straight blades.

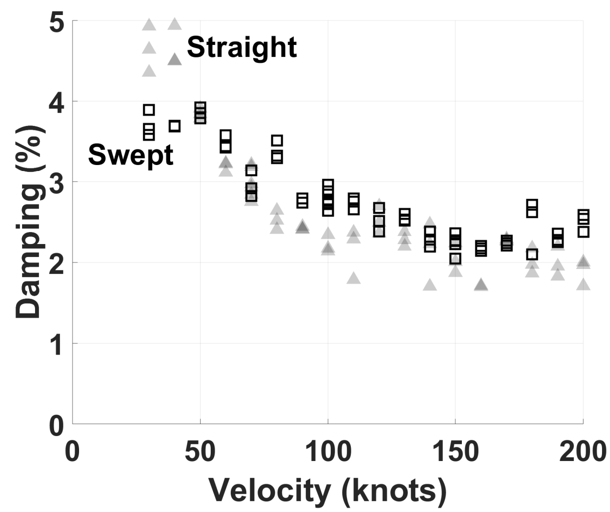

Figure 43: Chord damping; swept versus straight blades.

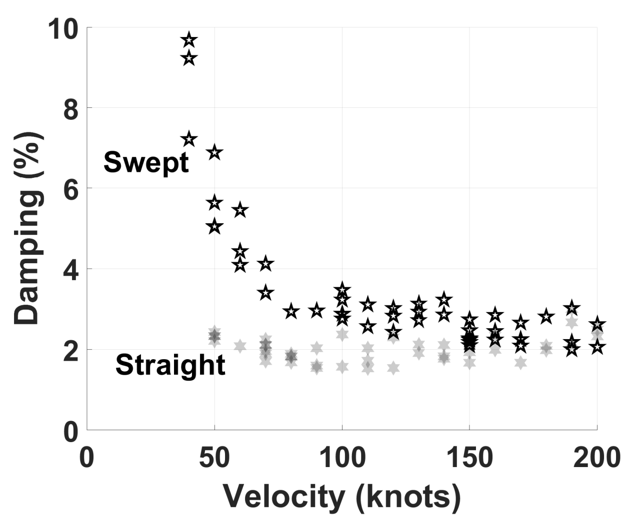

Figure 44: Torsion damping; swept versus straight blades.

affecting chord and hub pitch (or airplane pitch) affecting torsion. In the chord mode the impact is positive—the damping increases. In the torsion mode the impact is negative—the damping decreases. Thus, overall, the hingeless hub would be more stable, but for torsion.

The increase in damping in chord mode was explained earlier by its proximity to the regressive lag. (The regressive lag of the gimballed hub is far away from the chord mode.) But how much is the contribution from the hub moment? This is the established in following section.

Hingeless versus gimbal-locked hub: To understand the relative contributions of regressive lag and hub roll moment, the hingeless hub data is compared with the gimbal-locked hub. The gimbal-locked hub is the gimballed hub, but with its gimbal locked. Locking the gimbal produces a very stiff-inplane hub with the regressive lag far away from the chord mode. Thus, only the hub roll moment effect would kick in. Figure 41 shows the damping in chord. It is clear that locking the gimbal produces only about half the damping as the hingeless hub, at least at the low speeds. This implies only half the damping is from the hub moment, the other half is from regressive lag. However at higher speeds, beyond 80 kt or so, locking the gimbal produces almost the same damping as the hingeless hub. This implies the damping is then mainly from the hub moment.

Straight versus swept-tip The hingeless hub data is now compared between the straight and swept-tip blades. Figures 42, 43, and 44 compare damping in beam, chord, and torsion modes respectively. In the beam mode there is no significant change. At 200 kt there appears to be an increase in damping but conclusions are premature with a single set of data points. In the chord mode there is no significant change either. The regressive lag is closer to the wing chord mode for both sets of blades—straight or swept—when compared to the gimballed hub. But the swept-tip puts it right on top of the torsion mode. This is seen in Fig. 44. The damping of the torsion mode increases significantly. Thus, in summary, the hingeless hub with the swept-tip blades appears to have the most damping.

CONCLUSIONS

A 4.75-ft diameter Froude-scaled hingeless hub tiltrotor model was developed and tested up to unprecedented speeds of 200 kt (corresponding to 468 kt full-scale) at the University of Maryland Glenn L Martin wind-tunnel. The model has interchangeable hubs, blades, and pylon center of gravity, allowing various parametric variations. Straight and swept-tip blades were tested. The pylon C.G. was moved aft and forward of the wing elastic axis. Beam, chord and torsion mode damping were measured. Based on this work the following key conclusions are drawn:

1. The hingeless hub, when equipped with swept-tip blades, has significantly higher stability than a gimballed hub with straight blades.
2. Hingeless hubs have higher stability in the chord mode than gimballed hubs. The chord stability is more than twice at speeds lower than 100 kts, and about 50% higher at 200 kts.
3. The interaction of the rotor low frequency lag with the wing modes, chord for straight and torsion for swept, significantly increases the stability of the mode.
4. The hingeless hub loses torsion stability significantly. But swept-tip blades can solve this drawback.
5. The stability in beam mode is comparable between the two hubs. Neither perturbation hub moments nor low-frequency lag interacted with this mode.
6. Comprehensive analysis has been able to capture the general trends for hingeless hub cases. But predictions were harder for the torsion mode and swept-tip blades. It captured the subtle low frequency regressive lag interactions with wing chord and torsion modes and how it changed with swept-tip blades.
7. The stability remained largely unaffected between pylon C.G. forward or backward. The forward C.G. case showed very high levels of scatter in torsion mode for reasons unclear at the present.

Future work will focus on Mach-scale rotor and powered flight.

ACKNOWLEDGMENTS

This work is carried out at the Alfred Gessow Rotorcraft Center, University of Maryland at College Park under the Army/Navy/NASA Vertical Lift Research Center of Excellence (VLRCOE) grant number W911W62120003 with technical monitoring from Mahendra Bhagwat and points of contact Tom Parham (Bell), Hyeonsoo Yeo and Seyhan Gul (Army), and Wayne Johnson (NASA). Fabrication and assembly was carried out with the assistance of Dave Privett of the Calspan Corporation. We also wish to thank Benjamin Strobel, Joseph Hussey, Kelin Torres, and Brandon Russell of the Glenn L Martin Wind Tunnel.

REFERENCES

1. Magee, J. P., and Alexander, H. R., “V/STOL Tilt Rotor Aircraft Study: Wind Tunnel Tests of a Full Scale Hingeless Prop/Rotor Designed for the Boeing Model 222 Tilt Rotor Aircraft,” NASA CR D222-100059-1, The Boeing Company—Vertol Division, April 1973.
2. “Advancement of Proprotor Technology, Task II-Wind-Tunnel Test Results (NASA Contract NAS 2-5386),” NASA CR 114363, Bell Helicopter Company, date unknown/around 1972.
3. Ham, N. D., Bauer, P., Lawrence, T., and Yasue, M., “A Study of Gust and Control Response of Model Rotor-Propellers in a Wind Tunnel Airstream,” NASA CR-137756, August 1975.
4. Ham, N. D., and Whiteaker, H., “A Wind-Tunnel Investigation of Tilt-Rotor Gust Alleviation System,” NASA CR-152264, January 1978.
5. Datta, A., Tsai, F., and Sutherland-Foggio, J., “Design of a New Tiltrotor Test Facility at the University of Maryland,” AIAA SciTech Forum, San Diego, CA, January 2019.
6. Tsai, F., Sutherland, J., Akinwale, A., Morin, A., Gul, S., and Datta, A., “Development and Whirl Flutter Test of the Maryland Tiltrotor Rig,” *Journal of the American Helicopter Society*, Vol. 69, (1), January 2024, pp. 1–15.
7. Sutherland, J., Tsai, F., and Datta, A., “Whirl Flutter Test of Swept-Tip Tiltrotor Blades,” *Journal of the American Helicopter Society*, Vol. 69, (1), January 2024, pp. 1–12.
8. Gul, S., and Datta, A., “Prediction and Validation of Whirl Flutter Data of the Maryland Tiltrotor Rig,” *Journal of the American Helicopter Society*, Vol. 69, (1), January 2024, pp. 1–11.
9. Akinwale, A., and Datta, A., “High Speed Whirl Flutter Tests of the Maryland Tiltrotor Rig,” Vertical Flight Society 79th Annual Forum, West Palm Beach, FL, May 16–18 2023.
10. Delgado, X., and Datta, A., “High Speed Whirl Flutter Tests of Swept-tip Rotor Blades,” Paper AIAA 2024-1851, SCITECH Forum, Orlando, FL, January 8–12 2024.
11. O’Brien, N., and Datta, A., “Aeroelastic Stability of a Hingeless Hub tiltrotor at High Speeds,” Vertical Flight Society 80th Annual Forum, Montréal, Québec, May 7–9 2024.
12. Gul, S., and Datta, A., “Development of an Aeromechanics Solver for Loads and Stability of Hingeless Tiltrotors,” *Journal of Aircraft*, Vol. 60, (1), January 2023, pp. 143–159.

13. Sutherland, J., Tsai, F., and Datta, A., “Fabrication, Testing, and 3D Comprehensive Analysis of Swept-Tip Tiltrotor Blades,” *Journal of the American Helicopter Society*, Vol. 68, (1), January 2023, pp. 1–17.